 ISSN 0267-8179. DOI: 10.1002/jqs.3094

JQS Journal of Quaternary Science QRA Quaternary Research Association

Coupling of VAMPERS within iLOVECLIM: experiments during the LGM and Last Deglaciation

DANIELLE C. KITOVER,[1] HANS RENSSEN,[1,2]* RONALD VAN BALEN,[1] JEF VANDENBERGHE[1] and DIDIER M. ROCHE[1,3]
[1]Department of Earth Sciences, Vrije Universiteit Amsterdam, Amsterdam, The Netherlands
[2]Department of Natural Sciences and Environmental Health, University of South-Eastern Norway, Bø, Norway
[3]Laboratoire des Sciences du Climat et de l'Environnement (LSCE), CEA/CNRS-INSU/UVSQ, Gif-sur-Yvette Cedex, France

Received 1 August 2017; Revised 30 November 2018; Accepted 16 January 2019

ABSTRACT: The VAMPERS (Vrije Universiteit Amsterdam Permafrost Snow Model) has been coupled within iLOVECLIM, an earth system model. This advancement allows the thermal coupling between permafrost and climate to be examined from a millennial timescale using equilibrium experiments during the Last Glacial Maximum (21 ka) and transient experiments for the subsequent deglaciation period (21–11 ka). It appears that the role of permafrost during both stable and transitional (glacial–interglacial) climate periods is seasonal, resulting in cooler summers and warmer winters by approximately ±2 °C maximum. This conclusion reinforces the importance of including the active layer within climate models. In addition, the coupling of VAMPERS also yields a simulation of transient permafrost conditions, not only for estimating areal changes in extent but also total permafrost gain/loss. © 2019 The Authors. *Journal of Quaternary Science* Published by John Wiley & Sons Ltd.

KEYWORDS: climate modeling; deglaciation; LGM; paleoclimate; permafrost.

Introduction

There is an abundance of observational studies which attribute degrading and/or warming of current permafrost to recent global warming (Hinzman *et al.*, 2005). Monitoring of permafrost site conditions in, for example, Alaska (Osterkamp and Jorgenson, 2006), Siberia (Romanovsky *et al.*, 2007), Canada (Smith *et al.*, 2005) and on the Tibetan Plateau (Cheng and Wu, 2007), have exemplified this relationship. However, aside from this direct permafrost response, there are also a number of climate feedbacks to consider from thawing permafrost. Examples of feedbacks are: (i) biogeochemical, such as the increase in atmospheric carbon emissions (Schaefer *et al.*, 2011); (ii) hydrological, such as shifts in the seasonal hydrological regime (Wang *et al.*, 2009); and (iii) thermal, such as effects on the land–atmosphere energy flux. In the third instance, the focus of this study, the frozen subsurface may serve as an additional heat source during freezing and a sink due to increased absorption of energy from the latent heat demands as it thaws (Poutou *et al.*, 2004). It is possible that this effect may serve as a negative feedback, dampening the warming trend. As almost 25% of the Northern Hemisphere is underlain by permafrost (Zhang *et al.*, 2003), the potential role of any climate feedback effects could be important. It is hence essential that climate models not only be able to simulate permafrost dynamics, but also to represent the effects on the energy exchange between the (sub)surface and the atmosphere.

Several authors have simulated permafrost response within a climate or earth system model (Schaefer *et al.*, 2011; Burke *et al.*, 2013; Slater and Lawrence, 2013). Koven *et al.* (2013) presented a review of the coupled earth system models that specifically implement permafrost thermal dynamics. Among the different model configurations, there are a number of differing parameters. The main ones include use of snow and/or organic layer(s), the calculation of latent heat, and calculation and determination of ground thermal conductivity. However, the maximum depth employed among all the reviewed models was limited, with none extending deeper than 44 m. Although it is advisable to match the subsurface depth to the time scale of interest (Alexeev *et al.*, 2007), Stevens *et al.* (2007) have recognized that climate models often do not place their lower boundary layer deep enough. As a result, there is an underestimated heat storage/release available in the terrestrial subsurface. As studies into the relationship between lower boundary depth and continental heat storage reveal, this misplacement can impact model simulations, hence causing discrepancies in the results (Smerdon and Stieglitz, 2006).

In simulations from Hartikainen (2006) and Delisle (1998), the time scale is longer (i.e. millennial), and therefore the simulations' depth interval is larger. These examples also apply the common 'post-process' approach (Riseborough *et al.*, 2008), where climate model results force the land surface conditions to predict permafrost extent and/or depth. Such models are limited as there is no feedback or returning effect on the climate from such changes; there is no coupling.

Up to this point we have mentioned two ends within the spectrum of permafrost modeling research: one side providing coupled simulations but with a shallow subsurface depth (appropriate for short time spans) while the other side performs offline simulations with a deeper subsurface (fitting for millennial time scales). The research presented in this work aims to bridge this gap by examining long-term permafrost changes using a coupled climate model configuration.

Because permafrost has a relatively slow thermal response (Lunardini, 1995), compared to other earth system components such as the atmosphere (hours to days), lakes/rivers (days) and mixed-layer ocean (months to years), it is appropriate to capture climate–permafrost coupling over millennia. Particularly for this work, we study the Last Glacial Maximum (LGM) and the subsequent deglaciation because the radiative forcings and boundary conditions are relatively well known. For our coupled climate system, these are (relative to pre-industrial times) the presence of large ice sheets (causing

*Correspondence: Hans Renssen, Department of Natural Sciences and Environmental Health, as above.
E-mail: hans.renssen@usn.no

lower sea levels, exposed land, large orography differences and extended surface albedo changes), different (and evolving) orbital configuration and lower greenhouse gas (GHG) concentrations (CO_2, CH_4 and N_2O).

During the LGM, ocean and terrestrial proxy records indicate that the global mean annual air temperature was approximately 3–4 °C lower than today (Schneider von Deimling *et al.*, 2006; Annan and Hargreaves, 2013). In the polar regions, East Antarctica was about 9–10 °C colder than today while Greenland was approximately 15 °C colder than today (Masson-Delmotte *et al.*, 2013). The last deglaciation extends approximately from the LGM (~21 ka) to the Holocene (~9 ka) and is marked by increasing summer insolation in the Northern Hemisphere, which resulted in increasing temperatures that caused the retreat of the Laurentide and Fennoscandian ice sheets, and higher CO_2 levels among other effects. The rise in air temperatures during the last deglaciation serves as the forcing which directly drives changes in permafrost distribution/thickness and allows constraint of the thermal feedback discussed above. Because the LGM is a common reference point for the last glacial period (Braconnot *et al.*, 2007) other studies have simulated permafrost distribution for this period as well (e.g. Jin *et al.*, 2007; Levavasseur *et al.*, 2011; Vandenberghe *et al.*, 2012; Saito *et al.*, 2013).

Here we present simulation results from both equilibrium and transient paleoclimate experiments using a coupled atmosphere permafrost component (ECBilt–VAMPERS) within iLOVECLIM, an earth system model of intermediate complexity. We first introduce the equilibrium experiments, simulating the LGM climate. From this state at 21 ka, transient experiments over the last deglaciation period are conducted to capture the thermal feedback of degrading permafrost. As we are focused on the long-term response, these transient experiments only include the 'slow' forcings, i.e. changes in orbital parameters, atmospheric GHG levels and ice sheet configuration. We couple a permafrost model within an earth system model and subsequently analyze experiments to infer the thermal role of permafrost during major periods of climate change.

This work is the next step to integrating VAMPERS within iLOVECLIM. Before the full coupling presented here, VAMPER was validated as a stand-alone, post-processing model (Kitover *et al.*, 2012, 2013). With this stand-alone set-up, experiments were previously done for both pre-industrial and LGM climates. Most recently, enhancements were made to include a snow pack layer and allow for varying parameters of the geothermal heat flux and generalized lithology (Kitover *et al.*, 2015a). A future step is to extend the model to include the mentioned biogeochemical and hydrological feedbacks.

Model description

iLOVECLIM

iLOVECLIM is an earth system model of intermediate complexity (EMIC). This class of climate models arose as an intermediate between the fully integrated general circulation models and simplified conceptual climate models (Claussen *et al.*, 2002). As a result, EMICs have the ability to simulate hundreds of thousands of years at a reasonable computational cost but also represent most of the natural earth system, particularly incorporating the components with slow feedback effects, such as ice sheets, vegetation and permafrost.

iLOVECLIM is a 'code fork' of LOVECLIM 1.2 (Goosse *et al.*, 2010), from which most of the physical climate components have been retained. Namely, these are the atmosphere, ocean and vegetation. Other components of iLOVECLIM were not activated here, including ice sheets, carbon cycle and water isotopes. This implies that the ice sheets were prescribed (see Model experiments). Different versions of LOVECLIM have successfully simulated past climates including the LGM (Roche *et al.*, 2007), the Holocene (Renssen *et al.*, 2005, 2009) and the last millennium (Goosse *et al.*, 2005). Each model component of LOVECLIM was originally developed separately and the reader is referred to Goosse *et al.* (2010) for a detailed description of atmosphere–ocean–vegetation components and coupling mechanisms. The atmosphere, land and permafrost components of iLOVECLIM use a T21 horizontal resolution that is roughly equivalent to $5.6^\circ \times 5.6^\circ$ latitude–longitude.

ECBilt, the atmospheric model (Opsteegh *et al.*, 1998), consists of a dynamic core with three vertical horizons at 800, 500 and 200 hPa. ECBilt also includes the land surface module to which VAMPERS is specifically coupled. The CLIO module (Goosse and Fichefet, 1999) is a 3-D ocean general circulation model with a free surface. It has $3^\circ \times 3^\circ$ horizontal resolution and 20 vertical layers. VECODE, the dynamic terrestrial vegetation model (Brovkin *et al.*, 1997), is similar to VAMPER(S) in that it was particularly designed for coupling to a coarse-resolution earth system model. It is a reduced-form dynamic global vegetation model that characterizes the land surface as either trees, grass or no vegetation (i.e. 'bare soil') and is computed at the same resolution as the ECBilt grid. The plant types may be represented fractionally within each gridcell.

VAMPERS

VAMPERS is a 1-D soil heat conduction model with phase change capability, approximated using a finite difference scheme. The soil vertical column comprises 100 layers which progressively become thicker with depth based on a logarithmic scale. The entire soil depth is 3000 m. Soil freeze/thaw is captured using the apparent heat capacity method (Zhang *et al.*, 2008) but specifically implemented with a smoother phase change transition approach borrowed from Mottaghy and Rath (2006). This method and associated model equations are described in Kitover *et al.* (2013).

At each time step, VAMPERS calculates the characteristics of the subsurface thermal properties for each layer throughout the profile based on per cent (un)frozen water content and temperature. Using these characteristics of thermal conductivity and heat capacity, a new temperature profile is calculated based on the variable surface forcing (land surface temperature) at the top and the (spatially varying) geothermal heat flow at the base, for each terrestrial grid cell without perennial ice cover. There is not yet groundwater hydrology implemented into VAMPERS so no water/convective heat is transferred between subsurface layers. Rather, the subsurface is assumed to be saturated, where the water content of each layer equals its void space (porosity). For grid cells with a presumed sandy lithology, porosity decreases with depth based on a common depth–porosity equation (e.g. Athy, 1930). For bedrock lithologies, porosity is assumed to be very low (0.1) and remains the same throughout depth. Equations and parameter sensitivity tests associated with VAMPERS are described in Kitover *et al.* (2013).

To match the minimalism of the land surface within ECBilt, VAMPERS only uses porosity and geothermal heat values to vary between each ECBilt grid cell. These values are derived from individual databases that are based on a reclassified version of the Global Lithological Map Database (Hartmann and Moosdorf, 2012) and median geothermal heat flux values

previously derived from a combination of measurements, modeling and correlation estimates (Davies, 2013). The use of these data and how they were repurposed for application in VAMPERS is discussed in Kitover *et al*. (2015a).

Since the original development of VAMPER (Kitover *et al*., 2012), two enhancements to VAMPER were discussed in Kitover *et al*. (2015a). One was the changeover from an annual to a sub-daily time step (4 h), allowing development of an active layer, which is the uppermost layer of ground that undergoes annual freezing and thawing. This adjustment was necessary for coupling to the land surface portion of ECBilt. The other development was the option of including snow as superficial layers between the ground and atmosphere interface, allowing the role of snow as an insulator to buffer propagation of air temperatures into the subsurface. This comparison was shown in Kitover *et al*. (2015a), which as expected decreased the depth of permafrost due to higher winter temperatures at the ground surface. Note that this additional snow option is where VAMPER was renamed VAMPERS. Snow is modeled as a single variable depth divided into three layers. The thermal conductivity and heat capacity of the snow is dependent on the snow density, which in turn is dependent on the amount of fresh snow and age/compaction of the old snow. Similar to the soil layers, the thermal characteristics of the snow are recalculated at each time step but are based on snow temperature and snow density.

Coupling

The integration of VAMPERS into iLOVECLIM is done through direct coupling within the iLOVECLIM atmosphere component ECBilt. Specifically, within ECBilt is the land-surface model, which computes the land surface temperature and development of the snow layer by solving the heat budget at a single soil layer. The temperature and snow of the land-surface model single soil layer serves as the ground surface forcing for VAMPERS. In return, VAMPERS computes a ground heat flux, which depending on the subsurface thermal regime may be either negative or positive, which is part of the land surface heat budget in ECBilt. The coupling mechanism between VAMPERS and ECBilt is shown conceptually in Fig. 1.

As a prior phase to the full coupling between ECBilt and VAMPERS, a number of one-way experiments were run to analyze the effect of the iLOVECLIM climate on permafrost distribution and extent. In Kitover *et al*. (2015a), the one-way coupling gave an estimate of permafrost thickness distribution in the Northern Hemisphere at the pre-industrial climate state, while in Kitover *et al*. (2015b), the same one-way coupling scheme was done for the LGM climate.

Model experiments

All experiments are performed globally (Table 1) but analyzed from the Northern Hemisphere perspective.

Equilibrium experiments

The first three experiments are performed under fixed 21-ka boundary conditions. This set-up includes atmospheric GHG concentrations that correspond to ice-core measurements, which means lowered levels of [CO_2], [CH_4] and [NO_2]. The orbital parameters correspond to 21-ka values described by Berger (1978) and the ice sheet forcing is from the simulations of Ganopolski and Calov (2011).

Starting at a stable LGM climate (~21-ka orbital forcings), VAMPERS (initialized at 0 m depth of permafrost) was coupled to ECBilt, where permafrost was then able to develop in response to ground temperature forcing. Using a 1-kyr repeating cycle of the LGM climate parameters and external orbital forcings, the ECBilt–VAMPERS coupling within iLOVECLIM is run in asynchronous mode for 10 000 model years. At re-equilibrated conditions, the newly coupled version was then run for another 1000 model years synchronized. Asynchronous coupling is a technique to conserve computer resources where certain model components are temporarily inoperative to allow other parts of the system components to 'catch up' to a certain climate state. In our case, we ran VAMPERS constantly while ECBilt was paused to allow permafrost time to respond to the LGM climate system. The concept of asynchronous coupling is described in further detail in McGuffie and Henderson-Sellers (2005) and specifically described in Kitover *et al*. (2015a) for the ECBilt–VAMPERS coupling.

The following is a description of the first three simulations: EQ_LGM, EQ_LGM_GEOF and EQ_LGM_VAMP. The experiment EQ_LGM establishes the LGM climate state without coupling to VAMPERS and is therefore the control run to which all other runs are compared. The second experiment, EQ_LGM_GEOF, is a sensitivity test for the atmosphere–land coupling mechanism between VAMPERS and ECBilt. This simulation includes the VAMPERS set-up with 100 layers, but incorporates the ground heat flux only as a function of the geothermal heat flux (assuming an equilibrated stable geothermal gradient). This implies that the impact of land surface temperatures on the thermal profile is excluded. The difference in simulated surface temperatures between EQ_LGM_GEOF and EQ_LGM, as shown in Supporting Information Fig. S1, thus quantifies solely the impact of the coupling through the geothermal heat flux on the surface climate. The third experiment, EQ_LGM_VAMP, utilizes the full ECBilt–VAMPERS coupling. Comparing climate and permafrost parameters of EQ_LGM_VAMP against EQ_LGM reveals any

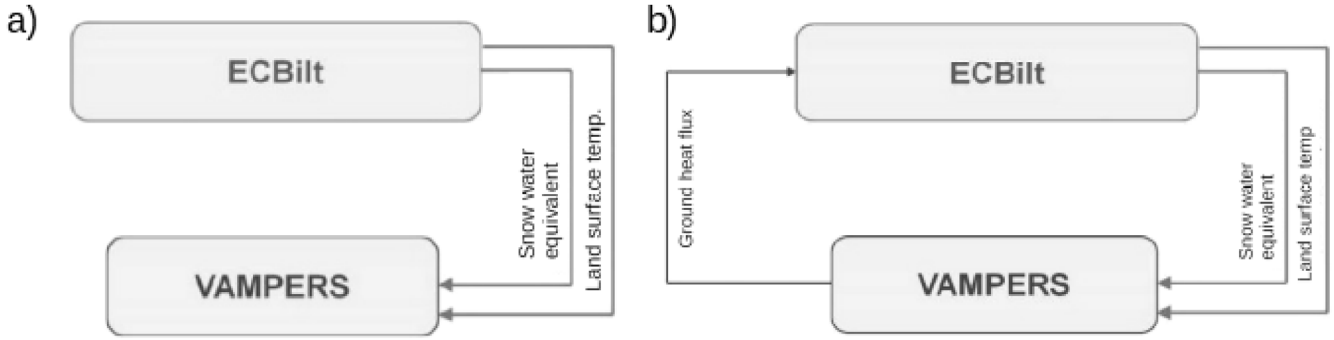

Figure 1. Description of the ECBilt–VAMPERS coupling scheme for the two equilibrium experiments: (a) EQ_LGM and (b) EQ_LGM_VAMP.

Table 1. Overview of experiments in this study. EQ_LGM are the equilibrium experiments and TR_DEGL are the deglaciation transient experiments.

	Experiment	ECBilt −VAMPERS coupling	Equilibrium/transient
1	EQ_LGM	No	Equilibrium (21 ka)
2	EQ_LGM_GEOF*	Yes	Equilibrium (21 ka)
3	EQ_LGM_VAMP	Yes	Equilibrium (21 ka)
4	TR_DEGL	No	Transient (21–11 ka)
5	TR_DEGL_VAMP	Yes	Transient (21–11 ka)

*GEOF, geothermal heat flux; this serves as a supplementary experiment; results are provided in Supplementary figures S1 and S2.

major effects on the equilibrated climate after coupling of VAMPERS to ECBilt. EQ_LGM_VAMP also gives the opportunity for an adequate spin-up to ensure soil temperatures are in equilibrium with the iLOVECLIM LGM climate before executing the transient runs.

A *t*-test was used to determine if there are any significant differences between the LGM climate state with and without the ECBilt–VAMPERS coupling. This standard approach tests the null hypothesis that two samples of climatic data (variances assumed to be unequal), namely surface air temperature, have the same parametric mean. Therefore, any observed changes in the LGM equilibrated climate that are attributed to coupling are significant at the 99% confidence level. The data sets which are compared for the *t*-test analysis are a 'snapshot' or moment in time (with each data set referencing the same point), and therefore detrending the data was not necessary. The temperatures of this analysis are the last 100 model years of the synchronized coupling simulation, which was in total 1000 years as described above. We did not take temporal autocorrelation into consideration.

Transient experiments

The two transient experiments, TR_DEGL and TR_DEGL_-VAMP, are the model runs without and with ECBilt–VAMPERS coupling, respectively. They cover the last deglaciation, beginning at the LGM (21 ka) to the early Holocene (11 ka). An accelerated forcing technique is used, where insolation, GHG concentrations and ice sheets are updated with an acceleration factor 10. This means that the time step of the boundary condition changes is accelerated ten times faster than a real-world time series. Given the difference in time scale of model components (several orders of magnitude different), this technique is used regularly for multi-millennial or longer simulations (McGuffie and Henderson-Sellers, 2005). A recent study by Varma *et al.* (2015) found that the effect of using the acceleration technique (×10) was negligible on the success of model-data comparison results for surface variables. However, they did suggest that in northern latitude ocean areas, biases in sea surface temperature evolution may occur. The insolation changes are a function of the orbital configuration (Milankovitch variations) and daily mean solar irradiance is calculated following Berger (1978). The GHG concentrations of CO_2, N_2O and CH_4 are time-dependent (Loulergue *et al.*, 2008; Lüthi *et al.*, 2008; Schilt *et al.*, 2010). Transient ice sheet forcing is from the simulations of Ganopolski and Calov (2011) using full realistic orbital and GHG forcing. During the simulated deglaciation, the Bering Strait remains closed and the effect of glacial–interglacial sea-level changes on bathymetry and on seawater salinity is neglected. Note that because we are interested in only long-term climate evolution, short-term forcings are not included in the transient experiment. However, we recognize that these changes, such as meltwater pulses (e.g. Licciardi *et al.*, 1999), volcanic eruptions (e.g. Zielinski *et al.*, 1997), dust fluxes (e.g. Mayewski *et al.*, 1997) and changes in solar activity (e.g. Muscheler and Beer, 2006), are also believed to have played a role in climate change during the last deglaciation.

Results and discussion

Equilibrium experiments

Climate analysis

Comparing the average annual surface temperature between [EQ_LGM] and [EQ_LGM_VAMP] shows that in the coupled experiment, the LGM climate is about 1 °C warmer in Eastern Russia and China while over the northern part of European Russia and eastern Canada, it is about 1 °C colder. From an overall perspective, aside from the general locations of the ice sheets, it appears that the Northern Hemisphere is predominantly warmer by about 0.5–1 °C (Fig. 2). This annual signal is probably the result of a reduction in the average temperature difference between summer and winter, as discussed below.

Compared to this annual signal, the coupling effect on surface air temperatures is much stronger in the results of the individual seasons (Fig. 3). During summer, there is latent heat consumption as the subsurface thaws, resulting in cooler conditions than without the coupling, while during winter, there is conversely a release of latent heat as it refreezes, producing warmer conditions. In the annual signal, these seasonal effects are largely cancelled out. This freezing/thawing process in turn affects the ground heat flux (out of the ground to the atmosphere), whereby there is a negative ground heat flux in spring/summer and a positive one in fall/winter (Fig. 3a). Even when permafrost is non-existent, the ECBilt–VAMPERS coupling captures a seasonally varying ground heat flux. Figure 4 shows the effect of thermal buffering occurring at both the high- and mid-latitudes, the latter of which primarily undergoes only annual ground freezing. This highlights the overall wider (global land surface) effect of coupling temporal variations of the geothermal gradient with the atmosphere. However, when comparing the latitudinal averages of daily ground heat flux at 20°N, 40°N, 60°N and 80°N, there is a more pronounced effect in the permafrost regions, namely 40–70°N (Fig. 4a). This corresponds to the geographical distribution of monthly surface air temperature anomalies, which shows an amplified effect at higher latitudes (Fig. 4b). At these parallels, the development of a pronounced active layer (Fig. 5), because of surface temperature forcing, is likely to have amplified the seasonal cycle of negative/positive ground heat fluxes. North of 70–75°N, the active layer is thinner and south of 20°N, the active layer is non-existent, so as expected the ground heat flux does not vary as much seasonally (Fig. 4a).

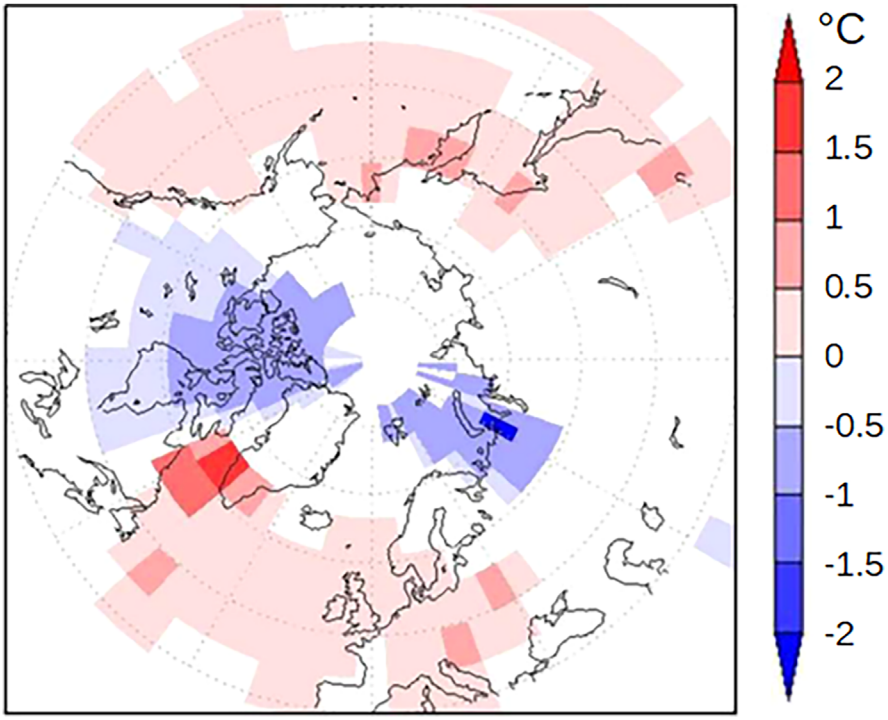

Figure 2. Significant differences in average annual surface air temperature between [EQ_LGM] and [EQ_LGM_VAMP].

Besides the impact of latent heat due to freezing and thawing, the inclusion of a deeper subsurface could potentially also have influenced the heat ground/atmosphere heat flux, because it increases the heat capacity of the terrestrial component within ECBilt. However, if this effect were significant, we would expect detectable changes in the atmospheric temperature due to the ECBilt–VAMPERS coupling outside the area with soil freezing and thawing. The absence of such an atmospheric response suggests that freezing and thawing is the dominant effect in the permafrost regions. The importance of freezing/thawing is confirmed by Mottaghy and Rath (2006), whose experiments in simulating both observed and synthetic borehole temperatures illustrate that inclusion of latent heat processes can play a significant role on the subsurface thermal regime.

The seasonality effect due to changing ground heat fluxes values will cause, according to the model results, an ~1–2 °C shift in average winter and summer temperatures. There is also a warming and cooling effect in spring and fall, respectively, but not as pronounced (only 0.5–1 °C) or as geographically widespread as in the other two seasons. This general effect of wintertime warming and summertime cooling is clear from an overall Northern Hemisphere perspective. However, the cooling occurring in Alaska and Canada cannot be directly attributed to local permafrost thaw because the overlying ice sheet decouples any heat transfer between the ground and atmosphere. Rather, it is likely that the summertime cooling in Eurasia caused shifting of atmospheric circulation patterns. Namely, there is a significant decrease in geopotential height (at 800 hPa) in eastern Siberia while over Alaska, the North Pacific and North Atlantic Oceans, there is a significant increase in geopotential height (Fig. 6c). The anomaly pattern points to a change in the large-scale circulation (Rossby waves), with a ridge over Alaska implying

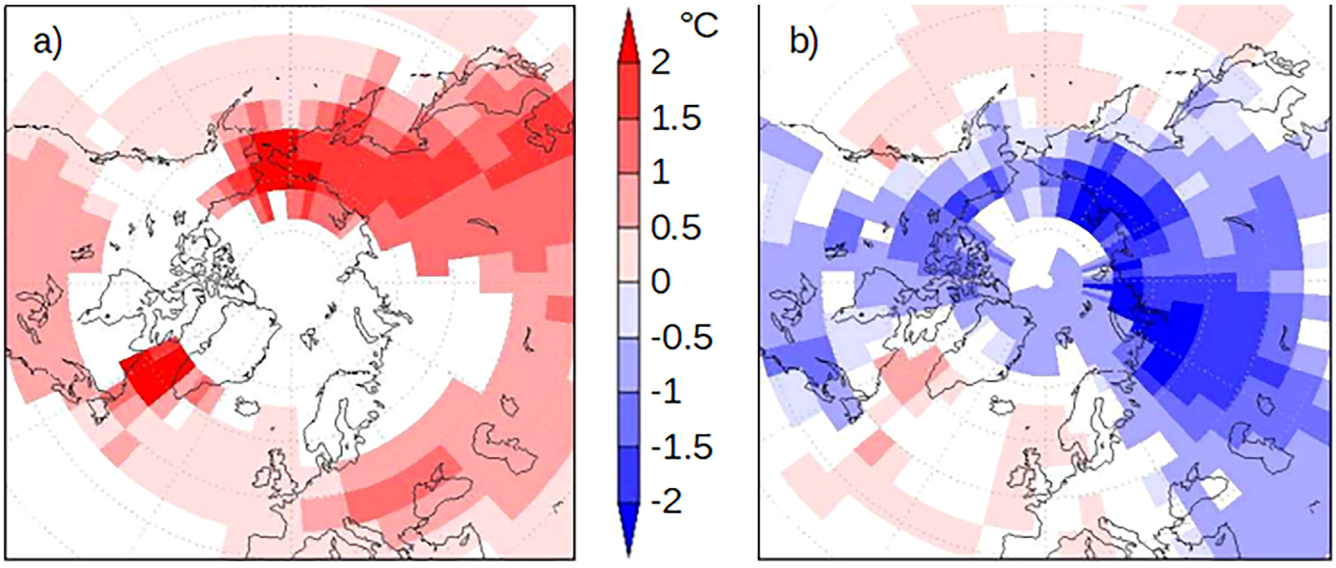

Figure 3. Significant seasonal temperature anomalies between [EQ_LGM_VAMP] and [EQ_LGM] for (a) winter and (b) summer.

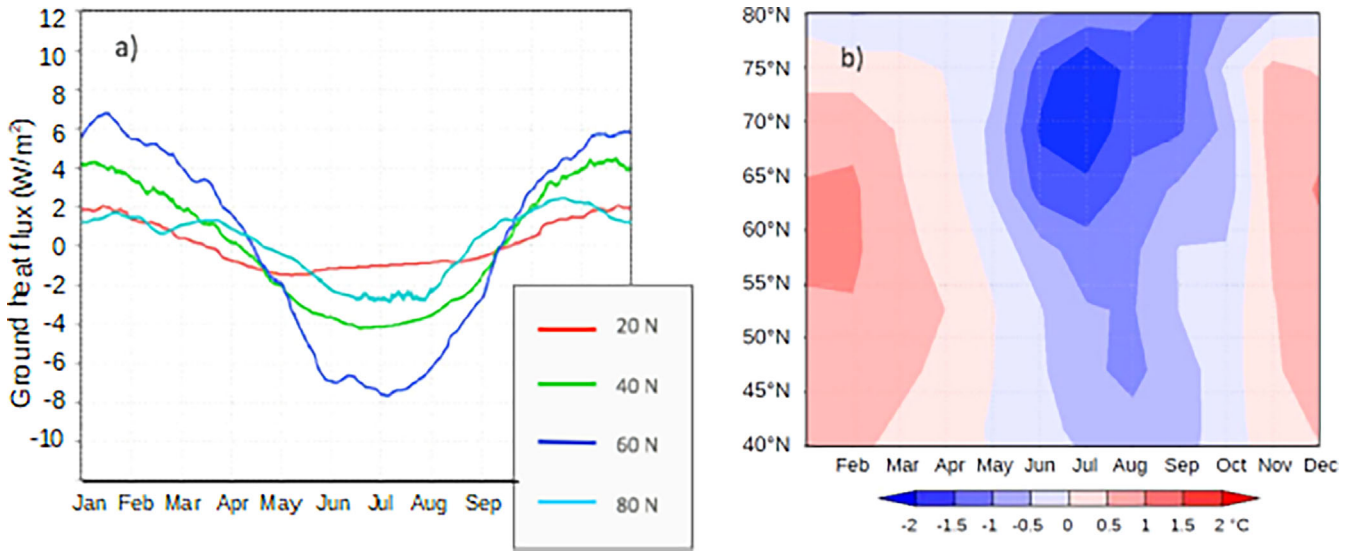

Figure 4. (a) Comparison of daily ground heat fluxes (W m^{-2}) from [EQ_LGM_VAMP] given as longitudinal averages (10°E to 180°E) at 20°N, 40°N, 60°N and 80°N latitude; (b) Hovmöller plot of averaged (10°E to 180°E) monthly surface temperature anomalies between [EQ_LGM_VAMP] and [EQ_LGM] over the latitude range 40–80°N.

a northerly flow that brings cold polar air to North America. These modifications in summer are particularly highlighted when compared to the other seasons, which show less changes to atmospheric circulation (Fig. 6).

Another geographical difference is the range of seasonal signal across Siberia, where in East Siberia there is both a strong summer and winter signal, whereas in European Russia there is a strong summer signal and an absent winter signal. The strength of the seasonal signal, aside from secondary influences such as shifts in atmospheric circulation, is primarily dependent on the ground heat flux. However, the ground heat flux is a function of the subsurface thermal gradient, where a steeper gradient produces a higher heat flux. Therefore, the geographical distribution of the seasonal signal can be traced to the annual range in surface air temperatures, where the greater range causes a stronger seasonal signal, particularly in summer and winter. From Fig. 7, it is clear that with increasing longitude eastward, the seasonal variation becomes greater. This longitudinal trend is an effect of continentality, which attributes a role of landmass on the seasonal temperature range. Note that the lack of winter signal in European Russia is also partially due to the high standard deviation, causing the results in this region to be statistically insignificant when applying the *t*-test (Fig. S2).

Permafrost analysis

The significant differences in modeled surface air temperature due to coupling with VAMPERS are strongest in the summer and winter periods (±1–2 °C). These cooling/warming effects

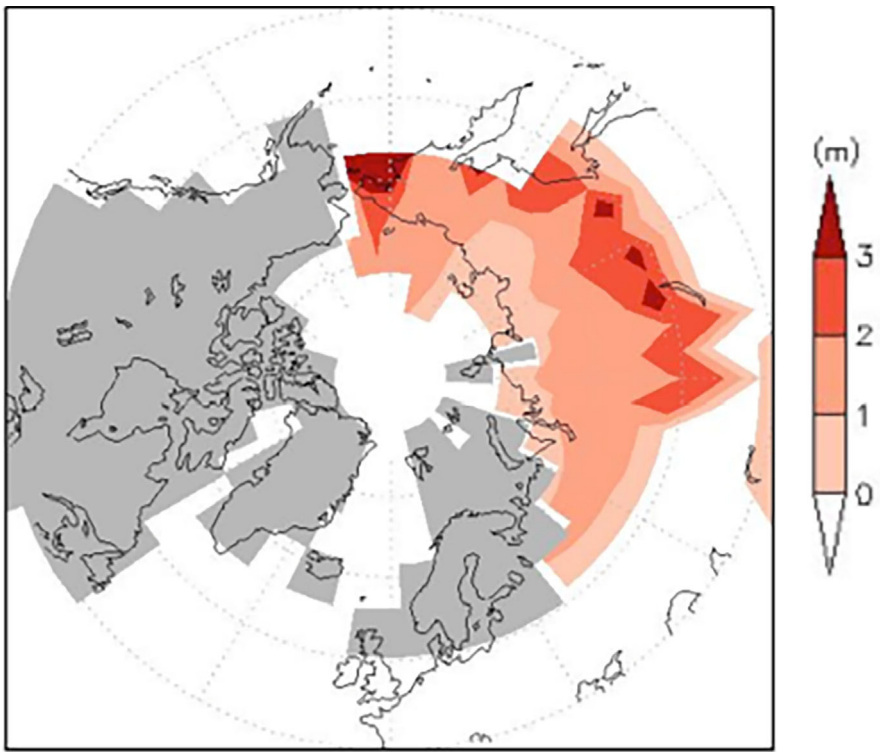

Figure 5. Average active layer depth (m) at 21 ka [EQ_LGM_VAMP].

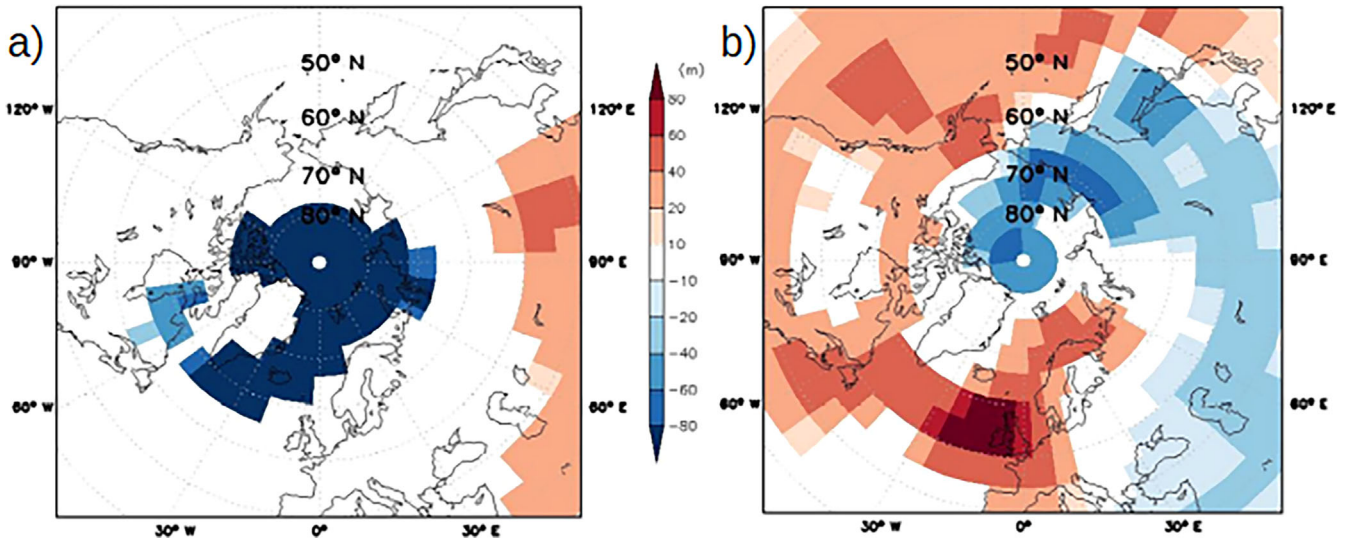

Figure 6. Significant differences in geopotential height at 800 hPa between [EQ_LGM_VAMP] and [EQ_LGM] for (a) winter and (b) summer.

also come through as an annual signal, but with less intensity (±0.5 °C). We note, in particular, annual forcing because it is strongly related to total permafrost depth (Williams and Smith, 1989). Subsequently, as there are indeed significant changes to the average surface air temperatures from the coupling process (Fig. 1), there are as expected corresponding changes to the simulated permafrost thickness and/or distribution. In the areas that showed an annual warming effect, permafrost is about 50–100 m thinner, whereas in areas that showed lower annual temperatures, permafrost is deeper by 10–50 m (Fig. 8c).

As the EQ_LGM is the control experiment, permafrost distribution in the EQ_LGM experiment is simulated by forcing an offline version of VAMPERS, forced by land surface temperatures from ECBilt. The permafrost thickness distribution modeled by EQ_LGM (Fig. 8a) and EQ_LGM_VAMP (Fig. 8b) is recognized as only continuous permafrost, rather than being able to model the full spatial extent that includes discontinuous and sporadic zones as well. This conclusion is borrowed and based on Kitover *et al.* (2015b), who assessed the VAMPERS-modeled LGM permafrost thickness distribution. Using proxy-based estimates as a reference, they found that the LGM simulated extent was underestimated, which they assert is probably due to the inability to capture the more sensitive regions of discontinuous permafrost. Therefore, given the close similarity in modeled permafrost distribution between the results of Kitover *et al.* (2015b) and this work (EQ_LGM and EQ_LGM_VAMP), we concludd that the permafrost distribution is also underestimated in the current experiment results.

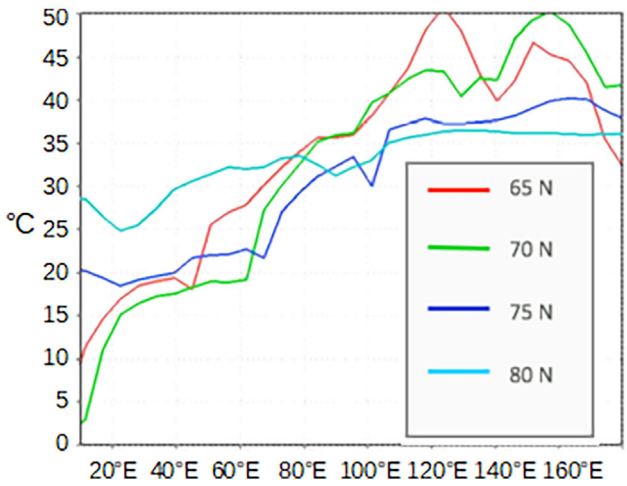

Figure 7. Difference in LGM summer–winter air surface temperatures (°C) from experiment EQ_LGM_VAMP, plotted against longitude. The different lines represent different latitudes in Eurasia.

Transient experiments

Climate analysis

To analyze the transient response of permafrost degradation on the climate, regional averages of summer and winter surface temperatures were calculated over the transient simulation. The eight sample regions (Alaska, Western Canada, Eastern Canada, European Plain, West Siberian Plain, Central Siberian Plain, East Siberia and Tibetan Plateau) cover most of the area underlain by permafrost during the LGM and subsequent deglaciation period. Similar to the conclusion from the equilibrium experiments, the transient simulations lead to a seasonal effect (i.e. winter warming and summer cooling) from coupling VAMPERS to ECBilt. This is illustrated in Fig. S3, which shows that all the selected regions (a to h) exhibit a consistent decrease in annual surface air temperature range (summer–winter). Another effect of the VAMPERS–ECBilt coupling seen in the transient experiment is the change in the transient warming trend, where there is a mild warming of approximately 0.2–0.5 °C (Fig. 9). This is a relatively small effect and rather than finding its cause directly in the permafrost thermal feedback, it is more likely to be due to disappearance of the ice sheets. As the ground is exposed, not only is permafrost able to develop but the geothermal heat flux is also newly coupled to the atmosphere. Although this contribution may seem small, our previous sensitivity experiments comparing temperature effects of only including the geothermal heat flux as the ground heat flux input for ECBilt was also about about 0.5 °C (Fig. S1).

It was originally hypothesized that as permafrost thaws and the active layer deepens during the last deglaciation, the additional energy required for this phase change produced a negative ground heat flux, potentially cooling the surface. To evaluate the magnitude of this effect, the average ground heat flux has been plotted over time (18–11 ka) per 10° parallel in Asia (Fig. 10a). It can clearly be seen that the ground heat flux becomes increasingly negative, particularly at 60–70°N,

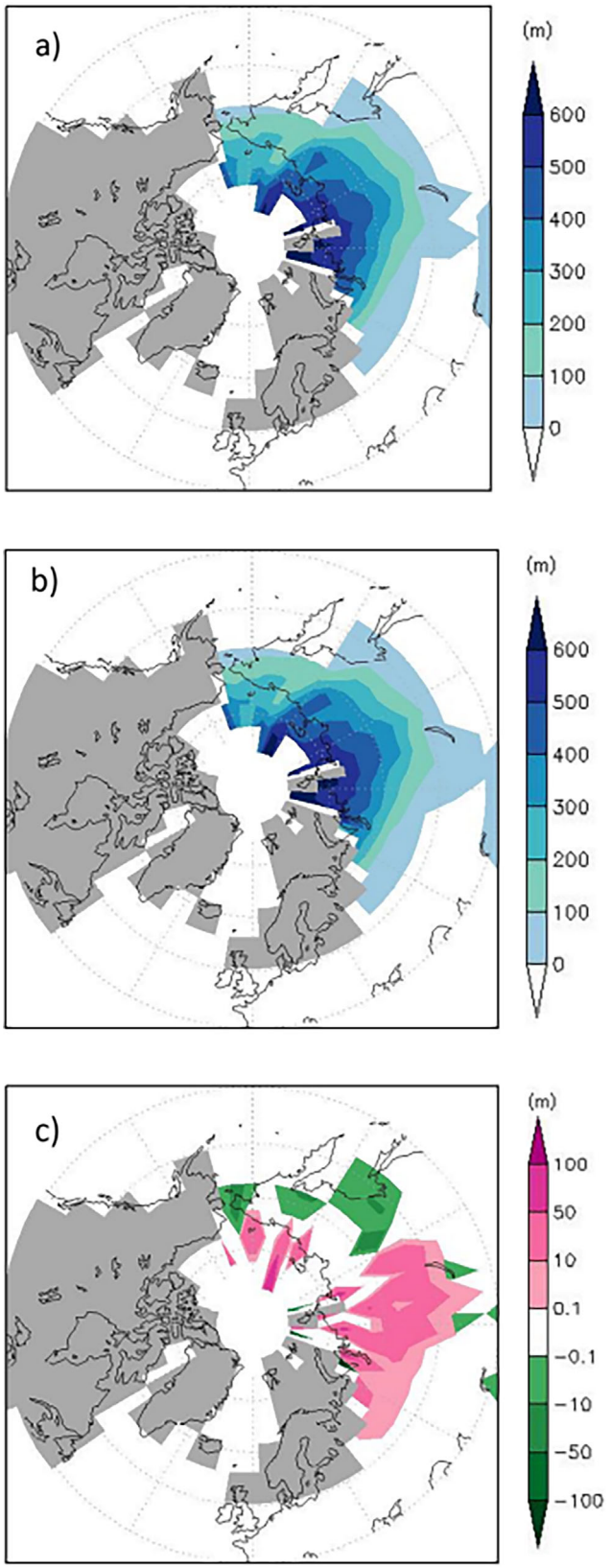

Figure 8. Permafrost thickness distribution (m) for (a) EQ_LGM and (b) EQ_LGM_VAMP, and (c) the difference between model runs [EQ_LGM_VAMP] – [EQ_LGM]. In (c), shading represents if more (pink) or less (green) permafrost developed in the coupled equilibrium experiment [EQ_LGM_VAMP] compared to the uncoupled version [EQ_LGM].

where most of the area is underlain by permafrost. By contrast, in Fig. 10(b), which shows the non-permafrost regions more to the south (0–30°N), there is much less variation in ground heat flux over time. Although these summary plots suggest that there is an impact on the ground heat flux during periods of permafrost thaw, it is apparently not strong enough to affect the climate beyond a few degrees centigrade. The average annual flux values ranged between 0.4 and $-0.4\,W\,m^{-2}$. Although these average values are comparable with observational studies (Tsuang, 2005), when weighed against other components of the surface heat budget in an Arctic environment, the ground heat flux makes up a relatively small portion (Westermann *et al.*, 2009).

Permafrost analysis

In our transient simulations, both permafrost degradation and disappearance occurred over the last deglaciation (Fig. S4). The percentage gain or loss of permafrost extent is calculated as the difference in per cent land area (Northern Hemisphere) underlain by permafrost. Note that in Fig. S4(a,c), the red line represents 21-ka permafrost delineation and the blue line represents 11-ka delineation. However, when there is no change in extent between 21 and 11 ka, the lines overlap (blue line overlaps red). Also calculated is a change in average permafrost thickness for the regions of Eurasia and North America, with accompanying histograms to show the frequency of grid cells with classed permafrost thicknesses (i.e. 50, 100, 150 m, etc.). The two measures, change in permafrost extent and change in permafrost thickness, reveal separate effects occurring during the deglaciation. Change in extent shows retreat or advancement of permafrost presence, whereas change in thickness reflects permafrost thawing or deepening.

In Eurasia, there was about a net 2% (20–22%) gain in Northern Hemisphere area underlain by permafrost. As this is quite a small change, there are a number of reasons to cause a seemingly minimal response, which we believe is probably underestimated. The first is that disappearance of permafrost extent (primarily on the southern margins) is countered by the gain of permafrost coverage on the Tibetan Plateau and the location of the former Fennoscandian ice sheet. The Tibetan Plateau in particular is unique as it is a region of continuous permafrost but is located much farther south than most of the occurrence in the Northern Hemisphere. As a result, the region shows some permafrost thaw while also showing permafrost gain. Its increase in permafrost coverage is likely to be due to the decrease in snow thickness (Fig. S5a), whereby ground temperatures are less insulated to freezing air temperatures. However, the warming in this region between 21 and 11 ka (Fig. S5b) also led to significant permafrost loss as well.

The second reason for an underestimate is that the simulated change of permafrost extent by iLOVECLIM does not take into account the flooding of continental shelves

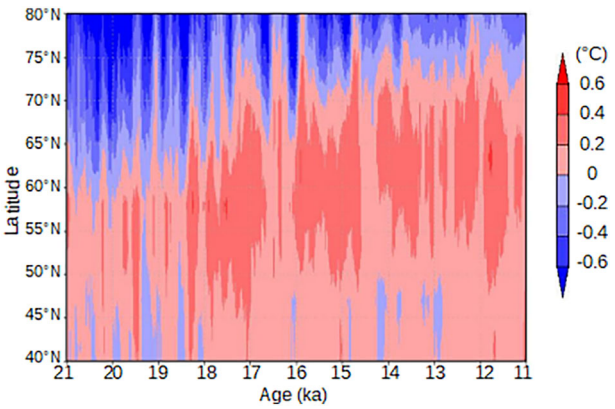

Figure 9. Differences [TR_DEGL_VAMP] – [TR_DEGL] in annual surface air temperatures (running mean) during transient simulation at 40–80°N, averaged for 10°E to 180°E.

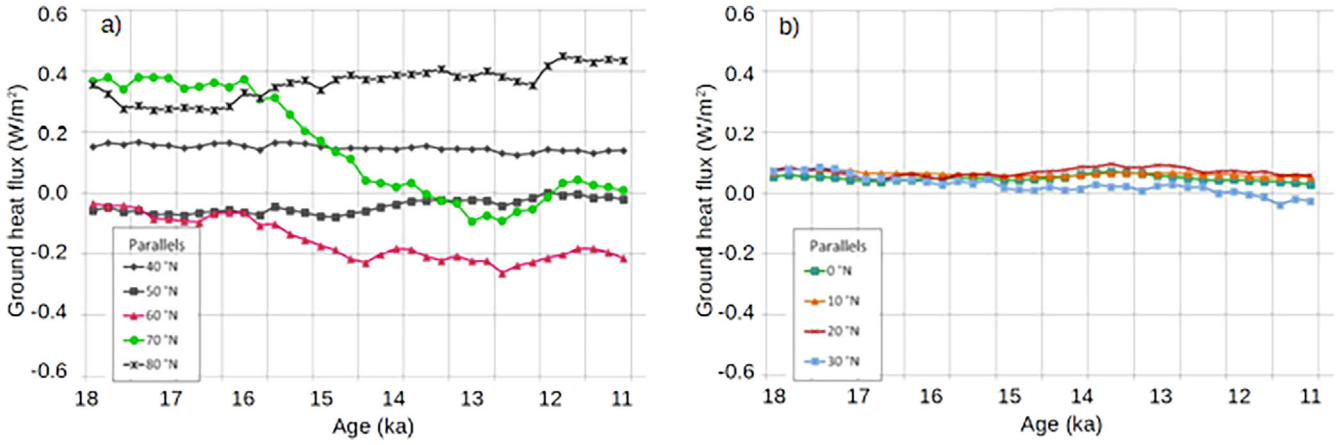

Figure 10. Average ground heat flux ($W\,m^{-2}$) over the transient simulation [TR_DEGL_VAMP] per 10° parallel in Asia. (a) Average at 40°N, 50°N, 60°N, 70°N, 80°N and (b) average at 0°N, 10°N, 20°N and 30°N.

during the deglaciation; hence the land–sea mask (reflecting the exposed land area during the LGM) used in the LGM experiment remains static during the transient run. This discrepancy is important to note because we model permafrost occurring on the East Siberian Arctic Shelf during the LGM but do not model its subsequent progression as subsea permafrost, some of which still currently exists today in the Laptev and East Siberian Seas (Romanovskii *et al.*, 2004). Crichton *et al.* (2014) estimate this loss of land area due to sea transgression since the LGM in the CLIMBER-2 model to be about $5–7 \times 10^6$ km^2.

Another reason for the underestimated response is that we only capture permafrost changes within the continuous zone. As noted previously, iLOVECLIM estimates of permafrost extent, in both an equilibrium and a transient state, are not able to reproduce discontinuous and sporadic occurrence. However, it is the unstable 'warmer' permafrost regions, found more often in the discontinuous regions (Smith and Riseborough, 2002), which are most sensitive to climate change (Romanovsky *et al.*, 2010). This point is exemplified by Vandenberghe *et al.* (2012), who used the mean annual air temperature isotherm to define the southern limit of discontinuous permafrost at the LGM and present-day. As a result, their estimated change in permafrost extent ('response') through these times, depending on their 'cold' or 'warm' simulation, is greater than our current transient simulation.

Despite a marginal loss of permafrost extent in Asia, the average permafrost thickness reduced from 319 m (standard deviation, $\sigma = 210$ m) to 286 m ($\sigma = 181$ m) deep. The change in grid cell frequency (bin classes 50, 100, 150 m, …, 1000 m) of permafrost thicknesses is shown in Fig. S6(a). There is a relatively large decrease in the frequency of permafrost cells with thin (<50 m) permafrost, which represents the areas that underwent total permafrost disappearance such as the southern margins in Russia. The increase in permafrost thickness, occurring within the middle range of permafrost thicknesses (100–500 m), represents the newly developed permafrost mostly in the Fennoscandia region and on the Tibetan Plateau. Finally, the frequency of cells with deep permafrost (>700 m) also decreases. This result demonstrates the need for climate models to account for both permafrost thickness and areal extent because analyzing only zonal loss would misleadingly show little permafrost response where the differences in permafrost thickness show a highly responsive change.

The above-mentioned discrepancies, which explain the probable cause of underestimating permafrost disappearance in Asia, also apply for the results in North America. Namely, at the very edge of Western Alaska and on the Bering land bridge, permafrost was present during the LGM (Fig. 8) but due to rising sea level, now exists as subsea relict permafrost (Osterkamp, 2007). Although this region is modeled to undergo permafrost degradation (as modeled by the green in Fig. S4d) there is no change in extent. In addition, the retreat of the Laurentide Ice Sheet also exposes the ground surface to arctic air temperatures. In turn, newly generated permafrost occurs in Alaska and Canada (Fig. S4c). Considering this behavior and again only representing changes in continuous permafrost, there was about a 7% (4–11%) increase in Northern Hemisphere land area underlain by permafrost.

The average permafrost thickness in North America decreased from 350 m ($\sigma = 207$ m) to 227 m ($\sigma = 117$ m). The thawing occurs mostly on the Bering land bridge and in southern Alaska. However, it is clear from the histogram of grid cell thicknesses (Fig. S6b) that there is a change in spread from wide-ranging values of permafrost thickness at 21 ka (i.e. one or two cells with thinner permafrost and a few cells with deeper permafrost) to the more frequently occurring mid-thickness values (100–500 m). This difference is expressed in the change in standard deviation of permafrost thickness from 207 to 117 m, indicating more frequently occurring thicknesses around the average depth of 227 m. These mid-range values mostly represent the newly formed permafrost at the location of the former Laurentide Ice Sheet. However, the permafrost that develops after retreat of the overlying ice sheet is not properly initialized and therefore causes an initial (non-equilibrated) overestimate of thickness, where in reality there was a slower growth of permafrost from the top down.

Permafrost evolution is illustrated for three different locations. The European Plain represents a case of completely disappearing permafrost (Fig. S7). Permafrost degradation occurs from the top and the bottom. The actual disappearance, rather than just warming, occurs between 17 and 16 ka. This degradation is quite rapid, averaging about $6\,cm\,a^{-1}$. However it may not be an unreasonable rate of loss if it is reflecting the rapid rate of warming set by the glacial–deglaciation transition. Further sensitivity studies would be required to analyze rates of warming with rates of degradation. In addition, it is probably not a linear relationship as the final stages of permafrost disappearance may be accelerated once the depth profile is sufficiently warm and isothermic. The complete disappearance in Europe matches with maps of modern permafrost extent, which shows no permafrost

currently existing in this area (Brown *et al.*, 2014). In addition, Kondratjeva *et al.* (1993) illustrate the late Quaternary estimates of the southern permafrost boundary in Russia which approximately correspond with our timing, as they show the boundary passing through this region (approx. 60° N, 60°E) between the late Pleistocene and the Holocene Climatic Optimum.

In West Siberia (Fig. S8), permafrost began to degrade from the top. Although thawing occurred only within a few meters from the surface, we expect this degradation to deepen for another 50–100 m throughout at least the next few thousand years. The deeper subsurface continues to absorb ground temperature disturbances well after the initial perturbation (ter Voorde *et al.*, 2014). As with the rapid response seen in the European Plain example, the near surface permafrost warms quite rapidly (Fig. S8b). Although there is little thaw simulated between 21 and 11 ka, the rapid rate of warming combined with the 'cold' permafrost suggests favorable conditions for development of relict permafrost. Due to a much colder initial climate state than, for example, in Eastern Russia, the rate of thaw lags behind the quick warming at the surface, causing a thermal imbalance. West Siberian relict permafrost is documented by Ananjeva *et al.* (2003), with the top of the permafrost about 50–100 m deep and total thickness varying between 10 and 150 m.

Other modeling results for transient paleo-permafrost simulations are difficult to directly compare with previous work because the experiments are site- or region-specific. For example, Lebret *et al.* (1994) and Delisle (1998) simulated permafrost depth changes over the last 100 000 and 50 000 years, respectively, in Western Europe. However, our model does not simulate any permafrost during the LGM for this region due to the ice sheet. Similarly, Hartikainen *et al.* (2010) simulated permafrost thickness changes in Scandinavia, also an area not recognized to have permafrost by iLOVECLIM. In Alaska, Osterkamp and Gosink (1991) simulated changes in permafrost depth over the last 100 000 years at Prudhoe Bay. During the LGM, our model assumes this area is covered by the ice sheet. However, what is consistent among all these previous studies and our current one is that the magnitude of response, with respect to the changes in thickness, are very similar. In general, the permafrost thaw rate is expected be around 0.1–1.5 cm a^{-1} according to Osterkamp and Gosink (1991). Similarly, we found as expected that cold permafrost degraded minimally at about 0.01 cm a^{-1} (East Siberia) while in areas of rapid warming at already 'warm' or unstable permafrost, degradation occurred about 6 cm a^{-1} (European Plain). However, as already mentioned, a further assessment of these results would require a sensitivity analysis to better understand rates/behavior of permafrost degradation in response to transient forcings.

Conclusions

This study presents the first results of a full thermal coupling between permafrost and climate using ECBilt–VAMPERS as a component within iLOVECLIM. The statistically significant differences between the equilibrated LGM climate with and without the thermal coupling, are ±1 °C annually and ±2 °C seasonally (warming in winter and cooling in summer). These differences resulted from introducing heat buffering (release and storage) within the near surface. The same magnitude of influence was seen consistently during the transient run where the coupled version resulted in lower summer and higher winter air surface temperatures. There was an observed effect on annual surface air temperatures during the deglaciation, shifting the warming trend by about +0.2 to 0.4 °C. Given this rather mild effect, it is difficult to directly link the cause(s), as it may be from the subsurface freeze/thaw response where the land surface is newly exposed and/or simply the coupling (i.e. added heat source) of geothermal fluxes to the atmosphere.

It was originally hypothesized that permafrost may serve as a heat sink during major periods of climate change due to latent heat demands as it thaws. However, there was no determinable signal from this process. Rather, the ECBilt–VAMPERS coupling produced only a seasonal signal, due to thermal buffering and freeze/thaw dynamics in the active layer. In addition, changes in surface air temperature at high latitudes were observed above regions that did not undergo freezing or active layer process. This is particularly evident in summer over Alaska and Arctic Canada, where a change in atmospheric circulation patterns resulted in anomalous northerly flow and cooling.

Over the deglaciation, permafrost in Asia disappeared primarily at the southern margins, but was offset by an increase in permafrost extent over parts of the Tibetan Plateau, probably due to changes in average snow depth, and the recently deglaciated regions of Fennoscandia. In North America, permafrost extent also resulted in a net increase of about 7% area underlain by permafrost due to deglaciated regions of Alaska and Canada. It must be considered that only continuous permafrost extent was simulated and that the continental shelves remained exposed throughout the modeled deglaciation; both probably contribute to a somewhat underestimated response of permafrost distribution to climate warming. Although average permafrost thickness reduced in both Eurasia (−31 m) and North America (−123 m), there was an increase in the frequency of grid cells having mid-range permafrost depths with a corresponding decrease in the frequency of grid cells with thin (<50 m) and deep permafrost occurrence (>500 m). This pattern indicates both a thawing response at the margins and in the deep permafrost zones, while also showing the development of new permafrost in the areas of previous ice cover.

Permafrost evolution over the last deglaciation is simulated and highlighted for two regions. On the European Plain in Russia, permafrost disappeared completely between 17 and 16 ka. This result corresponds with the modern state of extent, which shows no current permafrost presence. In West Siberia, the rapid warming and cold permafrost illustrate the beginning of relict permafrost formation. It is expected that a continued simulation using VAMPERS would illustrate further thaw from the top and decoupling between the frozen subsurface and surface conditions.

A future modeling improvement would be to couple VAMPERS with the ice sheet component in iLOVECLIM, as was recently done in the CLIMBER-2 model (Willeit and Ganopolski, 2015). Such a coupling would combine the impacts of varying properties of ice sheet thickness, local ground heat flux and surface climate, and would result in a more realistic simulation of permafrost occurrence and thickness under ice sheets and following deglaciation. In addition, examining the behavior and degradation rates of permafrost disappearance (which is probably not linearly correlated to warming rates) over different millennial-scale climate change scenarios is another interesting question for future research.

Acknowledgements. This work was supported by funds from the Netherlands Organization for Scientific Research, project no: 817.01.013.

Supporting Information

Additional supporting information may be found in the online version of this article at the publisher's web-site:

Figure S1. Significant difference in average annual surface air temperatures between [EQ_LGM_GEOF] – [EQ_LGM].

Figure S2. a) Standard deviation of winter surface air temperatures b) (Non)significant differences in average winter surface air temperatures between [EQ_LGM_GEOF] – [EQ_LGM].

Figure S3. Regional difference between average summer and average winter transient surface air temperatures plotted against age (in ka), covering the deglaciation from 21 ka to 11 ka. The dark dashed line represents without coupling [TR_DEGL] and the gray line is the coupled version [TR_DEGL_VAMP].

Figure S4. Changes in a) permafrost delineation (red = 21 ka, blue = 11 ka) for Asia b) permafrost thickness for Asia, c) permafrost delineation (red = 21 ka, blue = 11 ka) for North America, and d) permafrost thickness for North America. Note for a) and c) that the blue may be overlapping red when there is no change in extent. Note for b) and d) that green indicates permafrost thaw and pink indicates permafrost deepening.

Figure S5. a) Change in annual average snow depth between 21 ka and 11 ka, b) Change in annual average surface air temperature between 21 ka and 11 ka.

Figure S6. Histogram showing frequency distribution of permafrost thickness classes (bins increasing in 50 m intervals) for a) Eurasia and b) North America.

Figure S7. a) Depiction of modeled annual-mean transient permafrost thickness, and b) temperature depth profiles for the European Plain in Russia (60°N, 60°E).

Figure S8. a) Depiction of modeled annual-mean transient permafrost thickness, and b) temperature depth profiles for West Siberia (64°N, 70°E).

Abbreviations. GHG, greenhouse gas; LGM, Last Glacial Maximum.

References

Alexeev VA, Nicolsky DJ, Romanovsky VE *et al.* 2007. An evaluation of deep soil configurations in the CLM3 for improved representation of permafrost. *Geophysical Research Letters* **34** [DOI: 10.1029/2007GL029536]

Ananjeva G, Melnikov E, Ponomareva O. 2003. Relict permafrost in the central part of Western Siberia. In *Proceedings of the Eighth International Conference on Permafrost*, Zurich, Switzerland, 21–25 July: A.A. Publishers, pp. 5–8.

Annan JD, Hargreaves JC. 2013. A new global reconstruction of temperature changes at the Last Glacial Maximum. *Climate of the Past* **9**: 367–376 [DOI: 10.5194/cp-9-367-2013].

Athy L. 1930. Density, porosity, and compaction of sedimentary rocks. *American Association of Petroleum Geologists Bulletin* **14**: 1–24.

Berger AL. 1978. Long-term variations of caloric insolation resulting from the earth's orbital elements. *Quaternary Research* **9**: 139–167 [DOI: 10.1016/0033-5894(78)90064-9].

Braconnot P, Otto-Bliesner B, Harrison S *et al.* 2007. Results of PMIP2 coupled simulations of the Mid-Holocene and Last Glacial Maximum – Part 1: experiments and large-scale features. *Climate of the Past* **3**: 261–277 [DOI: 10.5194/cp-3-261-2007].

Brovkin V, Ganopolski A, Svirezhev Y. 1997. A continuous climate-vegetation classification for use in climate-biosphere studies. *Ecological Modelling* **101**: 251–261 [DOI: 10.1016/S0304-3800(97)00049-5].

Brown J, Ferrians O, Heginbottom JA, Melnikov E. 2014. Circum-Arctic Map of Permafrost and Ground-Ice Conditions. National Snow and Ice Data Center: Boulder, CO.

Burke EJ, Dankers R, Jones CD *et al.* 2013. A retrospective analysis of pan Arctic permafrost using the JULES land surface model. *Climate Dynamics* **41**: 1025–1038 [DOI: 10.1007/s00382-012-1648-x].

Cheng G, Wu T. 2007. Responses of permafrost to climate change and their environmental significance, Qinghai–Tibet Plateau. *Journal of Geophysical Research* **112** [DOI: 10.1029/2006jf000631].

Claussen, M, Mysak L, Weaver A, *et al.* 2002. Earth system models of intermediate complexity: closing the gap in the spectrum of climate system models. *Climate Dynamics* **18**: 579–586 [DOI: 10.1007/s00382-001-0200-1].

Crichton KA, Roche DM, Krinner G *et al.* 2014. A simplified permafrost-carbon model for long-term climate studies with the CLIMBER-2 coupled earth system model. *Geoscientific Model Development* **7**: 3111–3134 [DOI: 10.5194/gmd-7-3111-2014].

Davies JH. 2013. Global map of solid Earth surface heat flow. *Geochemistry, Geophysics, Geosystems* **14**: 4608–4622 [DOI: 10.1002/ggge.20271].

Delisle G. 1998. Numerical simulation of permafrost growth and decay. *Journal of Quaternary Science* **13**: 325–333 [DOI: 10.1002/(SICI)1099-1417(199807/08)13:4<325::AID-JQS385>3.0.CO;2-A].

Ganopolski A, Calov R. 2011. The role of orbital forcing, carbon dioxide and regolith in 100 kyr glacial cycles. *Climate of the Past* **7**: 1415–1425 [DOI: 10.5194/cp-7-1415-2011].

Goosse H, Brovkin V, Fichefet T *et al.* 2010. Description of the Earth system model of intermediate complexity LOVECLIM version 1.2. *Geoscientific Model Development* **3**: 603–633 [DOI: 10.5194/gmd-3-603-2010].

Goosse H, Fichefet T. 1999. Importance of ice–ocean interactions for the global ocean circulation: A model study. *Journal of Geophysical Research* **104**: 23337–23355 [DOI: 10.1029/1999JC900215].

Goosse H, Renssen H, Timmermann A *et al.* 2005. Internal and forced climate variability during the last millennium: a model-data comparison using ensemble simulations. *Quaternary Science Reviews* **24**: 1345–1360 [DOI: 10.1016/j.quascirev.2004.12.009].

Hartikainen J. 2006. *Numerical Simulation of Permafrost depth at Olkiluoto*. Laboratory of Structural Mechanics Helsinki University of Technology.

Hartikainen J, Kouhia R, Wallroth T. 2010. *Permafrost Simulations at Forsmar using a Numerical 2D Thermo-Hydro-Chemical Model. TR 09–17*. Swedish Nuclear Fuel and Waste Management Company: Stockholm.

Hartmann J, Moosdorf N. 2012. The new global lithological map database GLiM: A representation of rock properties at the Earth surface. *Geochemistry, Geophysics, Geosystems* **13**: n/a–n/a [DOI: 10.1029/2012GC004370].

Hinzman LD, Bettez ND, Bolton WR *et al.* 2005. Evidence and implications of recent climate change in northern Alaska and other arctic regions. *Climatic Change* **72**: 251–298 [DOI: 10.1007/s10584-005-5352-2].

Jin HJ, Chang XL, Wang SL. 2007. Evolution of permafrost on the Qinghai-Xizang (Tibet) Plateau since the end of the Late Pleistocene. *Journal of Geophysical Research* **112** [DOI: 10.1029/2006JF000521].

Kitover D, Renssen H, van Balen R *et al.* 2012. Modeling permafrost response of the Last Glacial Termination: first results of the VAMPER model. In *Proceedings of the 10th International Conference on Permafrost*, Salekhard, Russia, 25–29 June. The Northern Publisher; 209–214.

Kitover D, van Balen R, Roche D, *et al.* 2015a. Advancement toward coupling of the VAMPER permafrost model within the Earth system model iLOVECLIM (version 1.0): description and validation. *Geoscientific Model Development* **8**: 1445–1460.

Kitover D, van Balen R, Vandenberghe J *et al.* 2015b. LGM permafrost thickness and extent in the Northern Hemisphere derived from the Earth System Model iLOVECLIM. *Permafrost and Periglacial Processes* **27**: 31–42.

Kitover DC, van Balen RT, Roche DM *et al.* 2013. New estimates of permafrost evolution during the last 21 k years in Eurasia using numerical modelling. *Permafrost and Periglacial Processes* **24**: 286–303 [DOI: 10.1002/ppp.1787].

Kondratjeva KA, Khrutzky SF, Romanovsky NN. 1993. Changes in the extent of permafrost during the late quaternary period in the territory of the former Soviet Union. *Permafrost and Periglacial Processes* **4**: 113–119 [DOI: 10.1002/ppp.3430040204].

Koven CD, Riley WJ, Stern A. 2013. Analysis of permafrost thermal dynamics and response to climate change in the CMIP5 earth system models. *Journal of Climate* **26**: 1877–1900 [DOI: 10.1175/JCLI-D-12-00228.1].

Lebret P, Dupas A, Clet M *et al*. 1994. Modelling of permafrost thickness during the late glacial stage in France: preliminary results. *Canadian Journal of Earth Sciences* **31**: 959–968 [DOI: 10.1139/e94-085].

Levavasseur G, Vrac M, Roche DM *et al*. 2011. Present and LGM permafrost from climate simulations: contribution of statistical downscaling. *Climate of the Past* **7**: 1225–1246 [DOI: 10.5194/cp-7-1225-2011].

Licciardi JM, Teller JT, Clark PU. 1999. Freshwater routing by the Laurentide Ice Sheet during the last deglaciation. In *Mechanisms of Global Climate Change at Millennial Time Scale*, Clark PU, Webb RS, Keigwin LD (eds). American Geophysical Union: Washington, DC; 177–201.

Loulergue L, Schilt A, Spahni R *et al*. 2008. Orbital and millennial-scale features of atmospheric CH_4 over the past 800,000 years. *Nature* **453**: 383–386 [DOI: 10.1038/nature06950] [PubMed: 18480822].

Lunardini V. 1995. *Permafrost formation time*. CRREL Report 95-8. Cold Regions Research and Engineering Laboratory: Hanover, NH.

Lüthi D, Le Floch M, Bereiter B *et al*. 2008. High-resolution carbon dioxide concentration record 650,000–800,000 years before present. *Nature* **453**: 379–382 [DOI: 10.1038/nature06949] [PubMed: 18480821].

Masson-Delmotte V, Schulz M, Abe-Ouchi A *et al*. 2013. Information from paleoclimate archives. In *Climate Change 2013: the Physical Science Basis. Contribution of Working Group I to the Fifth Assessment Report of the Intergovernmental Panel on Climate Change*, Stocker TF, Qin D, Plattner GK, *et al.*, eds. Cambridge University Press: Cambridge.

Mayewski PA, Meeker LD, Twickler MS *et al*. 1997. Major features and forcing of high-latitude northern hemisphere atmospheric circulation using a 110,000-year-long glaciochemical series. *Journal of Geophysical Research* **102**: 345–326, 366.

McGuffie K, Henderson-Sellers A. 2005 *Climate Modelling Primer* 3rd edn. Wiley: Chichester.

Mottaghy D, Rath V. 2006. Latent heat effects in subsurface heat transport modelling and their impact on palaeotemperature reconstructions. *Geophysical Journal International* **164**: 236–245 [DOI: 10.1111/j.1365-246X.2005.02843.x].

Muscheler R, Beer J. 2006. Solar forced Dansgaard/Oeschger events? *Geophysical Research Letters* **33** [DOI: 10.1029/2006GL026779].

Opsteegh JD, Haarsma RJ, Selten FM *et al*. 1998. ECBILT: a dynamic alternative to mixed boundary conditions in ocean models. *Tellus A* **50**: 348–367 [DOI: 10.1034/j.1600-0870.1998.t01-1-00007.x].

Osterkamp TE. 2007. Characteristics of the recent warming of permafrost in Alaska. *Journal of Geophysical Research* **112** [DOI: 10.1029/2006JF000578].

Osterkamp TE, Gosink JP. 1991. Variations in permafrost thickness in response to changes in paleoclimate. *Journal of Geophysical Research* **96**: 4423–4434 [DOI: 10.1029/90JB02492].

Osterkamp TE, Jorgenson JC. 2006. Warming of permafrost in the Arctic National Wildlife Refuge, Alaska. *Permafrost and Periglacial Processes* **17**: 65–69.

Poutou E, Krinner G, Genthon C *et al*. 2004. Role of soil freezing in future boreal climate change. *Climate Dynamics* **23**: 621–639 [DOI: 10.1007/s00382-004-0459-0].

Renssen H, Goosse H, Fichefet T *et al*. 2005. Simulating the Holocene climate evolution at northern high latitudes using a coupled atmosphere–sea ice–ocean–vegetation model. *Climate Dynamics* **24**: 23–43 [DOI: 10.1007/s00382-004-0485-y].

Renssen H, Seppä H, Heiri O *et al*. 2009. The spatial and temporal complexity of the Holocene thermal maximum. *Nature Geoscience* **2**: 411–414 [DOI: 10.1038/ngeo513].

Riseborough D, Shiklomanov N, Etzelmüller B *et al*. 2008. Recent advances in permafrost modelling. *Permafrost and Periglacial Processes* **19**: 137–156 [DOI: 10.1002/ppp.615].

Roche DM, Dokken TM, Goosse H *et al*. 2007. Climate of the Last Glacial Maximum: sensitivity studies and model-data comparison with the LOVECLIM coupled model. *Climate of the Past* **3**: 205–224 [DOI: 10.5194/cp-3-205-2007].

Romanovskii N, Hubberten H-W, Gavrilov A *et al*. 2004. Permafrost of the east Siberian Arctic shelf and coastal lowlands. *Quaternary Science Reviews* **23**: 1359–1369 [DOI: 10.1016/j.quascirev.2003.12.014].

Romanovsky VE, Drozdov DS, Oberman NG *et al*. 2010. Thermal state of permafrost in Russia. *Permafrost and Periglacial Processes* **21**: 136–155 [DOI: 10.1002/ppp.683].

Romanovsky VE, Sazonova TS, Balobaev VT *et al*. 2007. Past and recent changes in air and permafrost temperatures in eastern Siberia. *Global and Planetary Change* **56**: 399–413 [DOI: 10.1016/j.gloplacha.2006.07.022].

Saito K, Sueyoshi T, Marchenko S *et al*. 2013. LGM permafrost distribution: how well can the latest PMIP multi-model ensembles perform reconstruction? *Climate of the Past* **9**: 1697–1714 [DOI: 10.5194/cp-9-1697-2013].

Schaefer K, Zhang T, Bruhwiler L *et al*. 2011. Amount and timing of permafrost carbon release in response to climate warming. *Tellus B* **63**: 165–180 [DOI:].

Schilt A, Baumgartner M, Schwander J *et al*. 2010. Atmospheric nitrous oxide during the last 140,000 years. *Earth and Planetary Science Letters* **300**: 33–43 [DOI: 10.1016/j.epsl.2010.09.027].

Schneider von Deimling T, Held H, Ganopolski A *et al*. 2006. Climate sensitivity estimated from ensemble simulations of glacial climate. *Climate Dynamics* **27**: 149–163 [DOI: 10.1007/s00382-006-0126-8].

Slater AG, Lawrence DM. 2013. Diagnosing present and future permafrost from climate models. *Journal of Climate* **26**: 5608–5623 [DOI: 10.1175/JCLI-D-12-00341.1].

Smerdon J, Stieglitz M. 2006. Simulating heat transport of harmonic temperature signals in the Earth's shallow subsurface: lower-boundary sensitivities. *Geophysical Research Letters* **33** [DOI: 10.1029/2006gl026816].

Smith SL, Burgess MM, Riseborough D *et al*. 2005. Recent trends from Canadian permafrost thermal monitoring network sites. *Permafrost and Periglacial Processes* **16**: 19–30 [DOI: 10.1002/ppp.511].

Smith M, Riseborough D. 2002. Climate and the limits of permafrost: a zonal analysis. *Permafrost Periglacial Processes* **13**: 1–15 [DOI: 10.1002/ppp.410].

Stevens MB, Smerdon JE, González-Rouco JF *et al*. 2007. Effects of bottom boundary placement on subsurface heat storage: implications for climate model simulations. *Geophysical Research Letters* **34** [DOI: 10.1029/2006GL028546].

ter Voorde M, van Balen R, Luijendijk E *et al*. 2014. Weichselian and Holocene climate history reflected in temperatures in the upper crust of the Netherlands. *Netherlands Journal of Geosciences – Geologie en Mijnbouw* **93**: 107–117 [DOI: 10.1017/njg.2014.9].

Tsuang B. 2005. Ground heat flux determination according to land skin temperature observations from *in situ* stations and satellites. *Journal of Hydrometeorology* **6**: 371–390 [DOI: 10.1175/jhm425.1].

Vandenberghe J, Renssen H, Roche DM *et al*. 2012. Eurasian permafrost instability constrained by reduced sea-ice cover. *Quaternary Science Reviews* **34**: 16–23 [DOI: 10.1016/j.quascirev.2011.12.001].

Varma V, Prange M, Schulz M. 2015. Transient simulations of the present and the last interglacial climate using a coupled general circulation model: effects of orbital acceleration. *Geoscientific Model Development Discussions* **8**: 5619–5641 [DOI: 10.5194/gmdd-8-5619-2015].

Wang G, Hu H, Li T. 2009. The influence of freeze–thaw cycles of active soil layer on surface runoff in a permafrost watershed. *Journal of Hydrology* **375**: 438–449 [DOI: 10.1016/j.jhydrol.2009.06.046].

Westermann S, Lüers J, Langer M *et al*. 2009. The annual surface energy budget of a high-arctic permafrost site on Svalbard, Norway. *The Cryosphere* **3**: 245–263 [DOI: 10.5194/tc-3-245-2009].

Willeit M, Ganopolski A. 2015. Coupled Northern Hemisphere permafrost–ice-sheet evolution over the last glacial cycle. *Climate of the Past* **11**: 1165–1180 [DOI: 10.5194/cp-11-1165-2015].

Williams P, Smith M. 1989 *The Frozen Earth*. Cambridge University Press: Cambridge.

Zhang T, Barry R, Knowles K *et al*. 2003. Distribution of seasonally and perennially frozen ground in the Northern Hemisphere. In

Proceedings of the Eighth International Conference on Permafrost, Zurich, Switzerland, 21–25 July. A. A. Balkema Publishers; 1289–1294.

Zhang Y, Carey S, Quinton W. 2008. Evaluation of the algorithms and parameterizations for ground thawing and freezing simulation in permafrost regions. *Journal of Geophysical Research* **113** [DOI: 10.1029/2007jd009343].

Zielinski GA, Mayewski PA, Meeker LD *et al*. 1997. Volcanic aerosol records and tephrochronology of the Summit, Greenland, ice cores. *Journal of Geophysical Research* **102**: 625–626, 640.

